# Theoretical study of spatiotemporal focusing for in-bulk laser structuring of dielectrics

Paul Quinoman, Benoît Chimier, Guillaume Duchateau

# Theoretical study of spatiotemporal focusing for in-bulk laser structuring of dielectrics

PAUL QUINOMAN[1], BENOÎT CHIMIER[1], AND GUILLAUME DUCHATEAU[1,2]

[1] University of Bordeaux-CNRS-CEA, Centre Lasers Intenses et Applications, 351 cours de la libération, UMR 5107, 33405 Talence, France
[2] CEA CESTA, 15 Avenue des Sablieres, CS60001, 33116 Le Barp Cedex, France; email: guillaume.duchateau@cea.fr

Compiled October 18, 2022

**For laser processing applications and creation of microstructures inside dielectric materials, focusing of femtosecond gaussian pulse within the bulk of these materials is commonly used. The laser energy is mainly absorbed in the focal spot due to the nonlinear feature of the laser-dielectric interaction. Recently, in order to get further control on the laser energy absorption, the spatiotemporal focusing technique, for which the pulse duration evolves in the course of propagation, have been introduced. However, the spatiotemporal focusing also leads to an inclination of the wavefront, the pulse-front tilt. In this work, the influence of the pulse-front tilt on the pulse propagation and interaction is studied by solving numerically the Maxwell's equations coupled to the laser induced electron dynamics in dielectrics. The qualitative behavior of the energy absorption, and geometric features of the resulting absorption volume are presented. By varying the laser intensity and pulse-front-tilt, both the aspect ratio and symmetry of absorption volume are changed. A simple model predicting the evolution of this aspect ratio is provided.** 

http://dx.doi.org/10.1364/ao.XX.XXXXXX

## 1. INTRODUCTION

Using femtosecond laser pulse to perform 3D micro- or nano-structures inside dielectric materials is of large interest for a wide range of applications, such as micro- and nano-photonics or micro- and nano-fluidics [1–3]. Due to the short pulse duration associated to the nonlinear feature of the laser-dielectric interaction process, focusing femtosecond laser pulses in the bulk of a dielectric makes possible to confine the laser energy absorption to the focal volume inside the material without damaging the surface. Depending on the laser pulse parameters, different material modifications can be induced, ranging from localized refractive index modifications to formation of nanovoids [1].

The laser micromachining of dielectric material results from laser ionization of valence band electrons toward conduction band, which will then absorb the incident laser energy before transferring it to the lattice. As a result, the irradiated matter can undergo phase transitions or structural modifications, leading to a localized structure. Due to the large band gap between valence and conduction bands, the absorption of light is nonlinear and occurs when the laser intensity becomes greater than a threshold intensity of the order of 10 TW/cm$^2$ [4]. Due to this nonlinear feature, the absorption volume and the resulting structure shape can be controlled by adjusting the laser parameters. Usually, the desired in-depth dielectric material modification is obtained by tuning the laser pulse duration, the pulse energy, the focusing numerical aperture (NA), the number of laser pulses or the spatial beam profile [5]. More recently, temporal focusing has been introduced to provide a new degree of freedom to manage the interaction [6] and control the absorption volume shape [7].

The spatiotemporal focusing technique, or simultaneous spatial and temporal focusing (SSTF), initially developed for two-photon microscopy [8], have been proposed to provide a better absorbed energy localization during in-bulk interaction [9]. Using this promising technique, the pulse duration decreases in the course of propagation toward the focal spot where it is minimal, providing an additional degree of freedom on the pulse intensity evolution. Several systems can be used to achieve spatiotemporal focusing, as presented in Ref. [10]. The ultra-short laser pulse broad spectrum undergoes angular dispersion, generally induced by a diffraction grating, that leads to spatial dispersion perpendicular to the propagation axis, i.e spatial chirp (SPC), during the pulse propagation. The wavelengths are spatially separated and the pulse local bandwidth is reduced, thus increasing its duration. After the beam collimation, an objective lens focuses the laser pulse, progressively overlapping the wavelengths and leading to the temporal focusing. The angular dispersion is also responsible for the appearance of a space-time inclination of the pulse-front, i.e. the so-called pulse-front tilt (PFT), and a wave front rotation (WFR) [11]. The presence of a PFT in the focal plane of the objective lens was shown to be an inherent feature of the SSTF technique, and cannot be compensated by introducing an input PFT in the system [12]. The PFT can influence the laser energy deposition, especially the shape and symmetry of the absorbing region [13]. The WFR was shown to also modify the interaction [14]. However, both are usually neglected to explain the observed resulting structures shapes [7, 15].

The present work aims at giving a qualitative understanding of the SSTF technique for in-bulk dielectric material modifications, by emphasizing the fundamental role of both the PFT and the pulse energy on the size and shape of the laser energy ab-

sorption volume. The propagation of such a laser pulse can be modeled using a three dimensional (3D) Nonlinear Schrödinger Equation [14]. However, it is valid only when light is scattered at small angles, assuming an electron density lower than the critical electron density. The 2D Maxwell's equations provide qualitative insight of the interaction [13], but are expected to modify the laser absorption and the geometry of the energy deposition. In this study, full 3D Maxwell's equations coupled to the electron dynamics are used to model the laser propagation and interaction (ARCTIC code [16]). A NA of 0.3 is considered to fulfill paraxial conditions in vacuum, and to develop the simple analytical model of focused tilted laser pulse presented in the manuscript. For higher numerical aperture, the paraxial approximation is no longer valid and polarization effects must be taken into account [17]. For this paraxial focusing condition, small material modifications are expected with a single laser pulse. Multi-pulse laser irradiation at high repetition rate must be used for material structuring [18]. The case of a PFT without WFR in the focal plane is considered as a representative case for the present study. This configuration can be obtained by adjusting the input temporal chirp before focusing, the laser pulse at the focus exhibits a PFT as the only spatiotemporal coupling [6]. This choice limits the free parameters and allow us to focus on the role of the PFT on the asymmetric interaction and to propose a method for the control of the aspect ratio of the structure.

In Sec. 2, the theoretical framework for the modeling is presented. In Sec. 2.A, the laser pulse spatiotemporal dynamics during SSTF is explained. Section 2.B presents the constitutive equations for the interaction with dielectric material. In Sec. 3, two main objectives are pursued, leading to two distinct studies. First, in Sec. 3.A, we aim at giving a qualitative insight about the interaction of a tilted femtosecond laser pulse within the bulk of fused silica. For this purpose, a numerical parametric study is achieved, using the Maxwell-solver code ARCTIC [16]. The absorption of the laser energy and the resulting asymmetry of the laser induced material modification are then discussed for various pulse energies and PFT. Then, in Sec. 3.B, a similar study is achieved for various pulse intensities near the interaction threshold, around 20 TW/cm$^2$ for fused silica [4]. The laser energy is lower compared with [13] and [14] because we seek for an energy deposition close to the focal spot, leading to smaller simulation domain. The geometric features of the absorbing region, i.e there dimensions and shapes, are investigated. An analytical expression is proposed in order to predict the deposited energy aspect ratio while using spatiotemporal focusing.

## 2. MODELING AND ASSUMPTIONS

This section presents the theoretical background for modeling the propagation of a spatio-temporally focused femtosecond laser pulse within dielectric material. First, the description of a focused femtosecond laser pulse exhibiting a PFT in the focal plane, is presented in Sec. A. The corresponding electric field will be introduced in the ARCTIC code [16] solving the Maxwell's equations coupled to electron dynamics in dielectric material, which is presented in Sec. B.

### A. Dynamics of focused titled laser pulse

By considering a laser pulse propagating along the $x$ axis and exhibiting a spatiotemporal coupling along the $z$ axis, the general form of the laser electric field envelop in the focal plane ($x = 0$) is given by [11]

$$E(x=0) = E_0 \exp\left[Q_{yy}y^2 + Q_{zz}z^2 + 2Q_{zt}zt - Q_{tt}t^2\right], \quad \textbf{(1)}$$

where $E_0$ is the peak amplitude of the electric field, the complex parameters $Q_{yy}$ and $Q_{zz}$ account for both beam width and curvature, $Q_{zt}$ for the spatiotemporal couplings, and $Q_{tt}$ for the pulse duration and temporal chirp. Note that only first order spatiotemporal couplings are considered, which is valid for relatively long pulse duration and/or moderate chirp at the objective lens. Especially, the second order spectral chirp, responsible for the further intensity localization for short enough laser pulses [10], is neglected. The real and imaginary part of $Q_{zt}$ represent the PFT and WFR, respectively [11]. Since only a PFT is considered in the focal plane in the present study, the parameters $Q_{yy}$, $Q_{zz}$, $Q_{zt}$ and $Q_{tt}$ are real for $x = 0$, and $Q_{zt}$ represents the PFT. The corresponding laser electric field in the focal plane then reads:

$$E(x=0) = E_0 \exp\left[-(y^2+z^2)/w_0^2 + 2Q_{zt}zt - t^2/\tau_0^2\right], \quad \textbf{(2)}$$

where $w_0$ is the beam waist and $\tau_0$ the pulse duration. It is convenient to introduce the dimensionless parameters $\bar{y} = y/w_0$, $\bar{z} = z/w_0$, $\bar{t} = t/\tau_0$ and $\gamma = 1 - (w_0\tau_0 Q_{zt})^2$, and write the electric field as

$$E(x=0) = E_0 \exp\left(-\bar{y}^2 - \bar{z}^2 + 2\sqrt{1-\gamma}\,\bar{z}\bar{t} - \bar{t}^2\right). \quad \textbf{(3)}$$

Note that $0 < \gamma \leq 1$ is required for the consistency of the field in Eq. (3), $\gamma \leq 0$ leading to split the pulse, $\gamma = 0$ to an infinite PFT, and $\gamma > 1$ to a complex value of $Q_{zt}$. The limiting value of the coupling term is then $Q_{zt} < 1/(w_0\tau_0)$, indicating the intuitive idea that the PFT is limited by the pulse duration and beam width. It is obvious at this point that the parameter $\gamma$ drives the whole spatiotemporal evolution of the laser pulse.

To describe the dynamics of the considered laser pulse, the general form of the electric field envelope for every $x$ position can be obtained by directly solving the paraxial wave equation [19] within the slowly varying envelope approximation for the electric field (3). The electric field evolution reads

$$E = E_0 f(\bar{x}) \exp\left[-f(\bar{x})(\bar{y}^2+\bar{z}^2)\right] \times \exp\left[2f(\bar{x})\sqrt{1-\gamma}\bar{z}\bar{t} - f(\bar{x})\,(1+i\gamma\bar{x})\,\bar{t}^2\right], \quad \textbf{(4)}$$

where $f(\bar{x}) = 1/(1+i\bar{x})$, and $\bar{x} = x/x_R$, where $x_R = n_0\pi w_0^2/\lambda_0$ is the Rayleigh length for the laser wavelength $\lambda_0$ and optical index $n_0$. For the considered laser pulse, the spatiotemporal intensity $I = \frac{1}{2}n_0\epsilon_0 c_0|E|^2$ profile is obtained from Eq. (4),

$$I = \frac{I_0}{\bar{w}^2(\bar{x})}\exp\left[-\frac{2(\bar{y}^2+\bar{z}^2)}{\bar{w}^2(\bar{x})} + \frac{4\sqrt{1-\gamma}\bar{z}\bar{t}}{\bar{w}^2(\bar{x})} - \frac{2\bar{t}^2}{\bar{\tau}^2(\bar{x})}\right], \quad \textbf{(5)}$$

where $I_0 = \frac{1}{2}n_0\epsilon_0 c_0 E_0^2$, and $\bar{w}(\bar{x}) = w(\bar{x})/w_0$ and $\bar{\tau}(\bar{x}) = \tau(\bar{x})/\tau_0$ are the relative pulse waist and duration evolution along the propagation axis, respectively. Those parameters are defined as the $1/e$ intensity width at $x$, in the spatial domain for $\bar{w}(\bar{x})$ and in the temporal domain for $\bar{\tau}(\bar{x})$, and reads:

$$w(\bar{x}) = w_0\sqrt{1+\bar{x}^2}, \quad \textbf{(6)}$$

$$\tau(\bar{x}) = \tau_0\sqrt{(1+\bar{x}^2)/(1+\gamma\bar{x}^2)}. \quad \textbf{(7)}$$

The spatiotemporal coupling term $\gamma$ in Eq. (7) induces an evolution of the pulse duration during the laser pulse propagation toward the focal plane. For higher values of the coupling $Q_{zt}$, leading to $\gamma \to 0$, the pulse duration follows the same relative evolution as the beam waist.

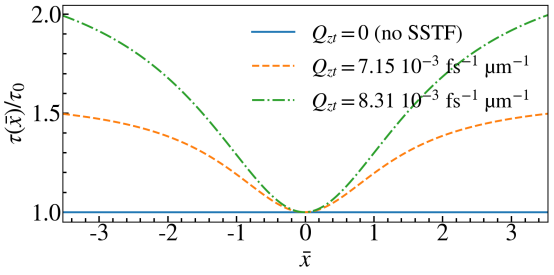


**Fig. 1.** Pulse duration evolution along the propagation axis $\bar{x} = x/x_R$, normalized by the focal plane pulse duration, for various values of the coupling term $Q_{zt}$.

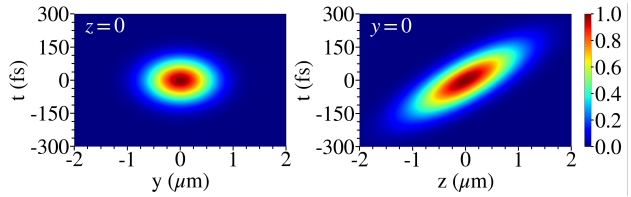


**Fig. 2.** Spatiotemporal intensity distribution in the focal plane for a 1 $\mu$m, 150 fs pulse (FWHM), tilted along the $z$ axis with $Q_{zt} = 7.15\ 10^{-3}$ $fs^{-1}\mu m^{-1}$, (left panel) intensity profile in the $(y,t)$ domain, (right panel) intensity profile in the $(z,t)$ domain.

Note that the longitudinal evolution of the intensity described by Eq. (5) does not depend on the coupling term $\gamma$, indicating that no further intensity localization is obtained for the boundary condition Eq. (3) where only first order spatiotemporal coupling was considered. This has been confirmed by solving the electric field propagation in the spatial and temporal Fourier domains.

The evolution of the relative pulse duration $\bar{\tau}(\bar{x})$ along the propagation axis $\bar{x}$ is presented in Fig. 1 for three different values of $Q_{zt}$ (see Eq. (2)). The full width at half maximum (FWHM) pulse waist and duration are 1 $\mu$m and 150 fs, respectively. The considered coupling term values are $Q_{zt} = 0$ (corresponding to a gaussian pulse without PFT), $Q_{zt} = 7.15 \times 10^{-3}$ fs$^{-1}\mu$m$^{-1}$, and $Q_{zt} = 8.31 \times 10^{-3}$ fs$^{-1}\mu$m$^{-1}$. The focal plane is located at $\bar{x} = 0$. The pulse duration increases with the distance from the focal spot in the presence of the spatiotemporal coupling. At $\bar{x} = -3.5$, the temporal stretch $\alpha = \tau(\bar{x})/\tau_0$ is $\alpha = 1.5$ for $Q_{zt} = 7.15 \times 10^{-3}$ fs$^{-1}\mu$m$^{-1}$, and $\alpha = 2$ for $Q_{zt} = 8.31 \times 10^{-3}$ fs$^{-1}\mu$m$^{-1}$. As expected, for a given waist and duration, higher PFT, represented by higher values of $Q_{zt}$, leads to a stronger evolution of the pulse duration. The spatiotemporal intensity distribution in the focal plane is presented in Fig. 2 for $z = 0$ (left panel) and $y = 0$ (right panel). The intensity profile domain clearly exhibits a tilt in the $(z,t)$ plane. The PFT angle is defined as the angle of the intensity distribution in the $(z,t)$ domain [11], and is $\theta_{PFT} = (1-\gamma)\tau_0/w_0$. In the focal plane, the beam waist along the $y$ direction at $z = 0$ is the same as the beam waist along the $z$ direction at $y = 0$, indicating the beam is cylindrical. However, due to the PFT, the transverse extension in the $z$ direction for an instant $t \neq 0$ is larger than its extension in the $y$ one for the instant $t \neq 0$. From the temporal point of view, the part of the pulse in the domain $z < 0$ will crosses the focal plane before the part of the pulse in the domain $z > 0$. During the interaction with the material, different electron dynamics are thus expected in the $(x,y)$ plane and in the $(x,z)$, contrary to conventional cylindrical gaussian pulse. Another way to characterize the influence of the PFT on the beam spatial

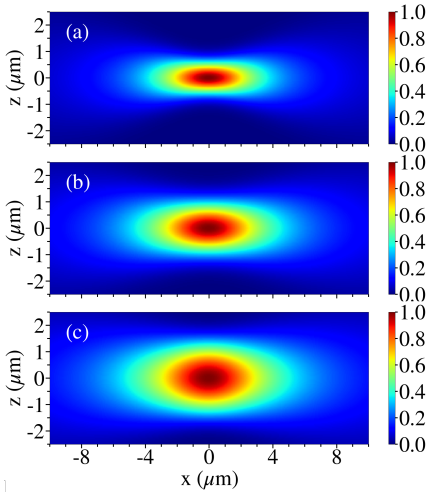


**Fig. 3.** Normalized laser fluence in the transverse-longitudinal domain for a gaussian pulse (a), chirped pulses along the $z$ axis with $Q_{zt} = 7.15\ 10^{-3}\ fs^{-1}\mu m^{-1}$ (b) and $Q_{zt} = 8.31\ 10^{-3}\ fs^{-1}\mu m^{-1}$ (c). The pulse propagates from the left to the right.

distribution is to consider the laser fluence. Since the fluence is the integrated intensity over time, it represents the average influence of the PFT. By integrating Eq. (5),

$$F = \frac{F_0/\sqrt{\gamma}}{\bar{w}(\bar{x})\bar{w}_{eff}(\bar{x})} \exp\left[-\frac{2\bar{y}^2}{\bar{w}^2(\bar{x})} - \frac{2\bar{z}^2}{\bar{w}^2_{eff}(\bar{x})}\right], \tag{8}$$

where $F_0 = \sqrt{\pi/2} I_0 \tau_0$ and $w_{eff}$ is the effective radius defined as the 1/e fluence transverse extension along the $z$ axis :

$$w_{eff}(\bar{x}) = w_0\sqrt{(1+\gamma\bar{x}^2)/\gamma}. \tag{9}$$

It clearly appears that the laser fluence in the $(y,z)$ domain exhibits an elliptic shape due to the spatiotemporal coupling. The difference between both transverse fluence distributions due to the spatiotemporal coupling indicates that the laser fluence transverse extension is longer in the $z$ direction than in the $y$ one. The normalized laser fluence in the $(x,z)$ domain is presented in Fig. 3 for a gaussian pulse ($Q_{zt} = 0$) (a) and chirped pulses with $Q_{zt} = 7.15\ 10^{-3}\ fs^{-1}\mu m^{-1}$ (b) and $Q_{zt} = 8.31\ 10^{-3}\ fs^{-1}\mu m^{-1}$ (c). The FWHM beam waist and duration are 1 $\mu$m and 150 fs, respectively. For each pulse, contrary to the intensity, the laser fluence is symmetric along the $z$ axis. However, the chirped pulse has a larger transverse extension, increasing with the $Q_{zt}$ value, i.e with the PFT. This extension shows the possibility to control the transverse size of the fluence profile by adjusting the PFT, and to control the aspect ratio of the laser induced material modifications. Finally, the longitudinal extension of the fluence profile is also extended, due to the variation of the pulse duration with the longitudinal coordinate $x$.

### B. Laser propagation and interaction with dielectric materials

The propagation of a single femtosecond laser pulse in fused silica is performed in 3D using the Maxwell solver code ARCTIC [16] accounting for the material evolution during the laser propagation. In the ARCTIC code, the Maxwell equations are coupled to a two-temperature model including the electron dynamics. The equations are discretized in the three spatial dimensions by means of Yee scheme [20], and the simulation domain includes

Bérenger's Perfectly-Matched-Layer absorbing boundary condition [21]. Since a femtosecond laser pulse interaction with dielectric material is considered, hydrodynamic relaxations and thermal conduction are neglected during the matter heating process, their characteristics timescales being in the ps and µs range, respectively [4].The electric field $\vec{\mathcal{E}}$ and magnetic field $\vec{\mathcal{B}}$ evolutions are calculated by solving the Maxwell equations

$$\nabla \wedge \vec{\mathcal{E}} = -\partial_t \vec{\mathcal{B}}, \tag{10}$$

$$\mu_0^{-1} \nabla \wedge \vec{\mathcal{B}} = \vec{J}_e + \vec{J}_i + \partial_t \vec{\mathcal{D}}, \tag{11}$$

with $\mu_0$ the vacuum permeability, $\vec{J}_e = -en_e\vec{u}_e$ the electron current density ($n_e$ and $\vec{u}_e$ are the electron density and velocity, respectively), and $J_i$ the effective ionization current [22]. The electric displacement $\vec{D}$ account for linear $\chi^{(1)}$ and nonlinear $\chi^{(3)}$ dielectric susceptibilities:

$$\vec{\mathcal{D}} = \epsilon_0 \left[1 + (n_n/n_{BV}) \left(\chi^{(1)} + \chi^{(3)}|\vec{\mathcal{E}}|^2\right)\right] \vec{\mathcal{E}}, \tag{12}$$

where $\epsilon_0$ is the vacuum permittivity, $n_n$ is the neutral density and $n_{BV}$ the initial neutral density. These equations are coupled to a two-temperature fluid model describing the electron dynamics and lattice heating. The equations for the density, momentum and energy of conduction band electrons are written as:

$$\partial_t n_e = W_{PI} + W_{Col} - n_e/\tau_r, \tag{13}$$

$$\partial_t \vec{u}_e = -e\vec{\mathcal{E}}/m_e - \vec{u}_e \nu_e, \tag{14}$$

$$\partial_t (n_e \xi_e) = m_e n_e u_e^2 \nu_e - 3/2 U_g W_{Col} - \gamma_{el}(T_e - T_l), \tag{15}$$

where $W_{PI}$ is the photoionization rate calculated from the Keldysh model [23], $W_{Col}$ is the collisional ionization rate described by using the Keldysh impact formula [24], $\tau_r$ is the characteristic time of electron recombination, $m_e$ is the electron mass, $\nu_e$ is the electron collision frequency and $U_g$ is the material bandgap. Note that solid fused silica was shown to present a band structure through ab initio calculations and experimental investigations [25]. Indeed, fused silica exhibits a local order despite its amorphous structure, allowing one to use the Keldysh theory to describe the photoionization process. The electron-lattice coupling term is $\gamma_{el} = (3/2) n_e k_B/\tau_{el}$, where $\tau_{el}$ is the electron-lattice relaxation time and the electron temperature is $T_e = 2\xi_e/(3k_B)$. The electron energy density in Eq. (15) neglects thermal diffusion process, because of the picosecond lifetime of the conduction electrons, which leads to a maximum diffusion length of less than 1 nm, considering electrons with an energy of a few eV. These maximum values are much smaller than the micrometer dimension of the beam waist. The lattice temperature $T_l$ is given by

$$C_l \partial_t T_l = \gamma_{el}(T_e - T_l). \tag{16}$$

with $C_l$ the lattice heat capacity. The total energy density $U_l$ absorbed by the material is calculated at the end of the simulation, at 2 ps, with the expression $U_l = C_l T_l$. At this time, the electron density is close to zero because of the electron recombination, such that no further energy transfer from the electrons to the lattice is possible. Note that the lattice temperature is not calculated as the total absorbed energy divided by $C_l$, because radiative electron recombination is considered. In this case, the energy transferred to the lattice only corresponds to the laser energy absorbed by the electrons. The ionization energy is assumed to be lost during processes like light emission or self-trapped exciton formation [26].

## 3. SIMULATIONS OF LASER STRUCTURING IN FUSED SILICA

The propagation of a single chirped pulse within fused silica is now considered by using the ARCTIC code presented above. The laser and material parameters used for simulations are presented in Tab. 1. The FWHM beam waist $\sqrt{2\ln 2} w_0 = 1$ µm corresponds to the numerical aperture $NA = \lambda_0/w_0\pi \simeq 0.3$.

The electron collision frequency and recombination time, and the electron-lattice relaxation time are set to constant values, with a reasonable order of magnitude [27]. For low pulse energy and numerical aperture, leading to a few eV electron energy [28] and a lattice heating below modification threshold, only smooth variations of these parameters are expected. The present study aims at investigating the influence of the spatial chirp on the behavior of the energy deposition. Small variations of the electron collision and relaxation time are thus not expected to significantly modify the results, and the shape of the energy deposition is mainly correlated to the electron density evolution (within the Drude model). Concerning the recombination process, the decay of the conduction band electrons in fused silica is a complex process, and may take place by radiative recombination with the emission of photons or defect formation like non-bridging oxygen-hole and self-trapped excitons [26]. Like in the main numerical studies on the laser-dielectric interaction, we choose to model the recombination rate by a single exponential decay term associated to the formation of self-trapped excitons as observed in experiments [29].

The chirp is along the $z$ axis and the considered time domain for a simulation depends on the chirp parameter. It is adjusted such that the instant where the peak intensity of the laser pulse reaches the calculation domain ($x = x_b$), is twice the FWHM pulse duration at the boundary, i.e $2\sqrt{2\ln 2}\tau(x_b)$, with $\tau(x_b)$ given by Eq. (7). Simulations are stopped when all the conduction electrons recombined. For the gaussian pulse, the peak intensity of the pulse reaches the boundary of the domain 300 fs after the beginning of the simulation, and the simulation lasts for 1 ps. For the most chirped pulse, it is 900 fs and the simulation is around 2 ps. The laser field in Eq. (2) is propagated in the material ($n_0 = 1.45$) without interaction in temporal and spatial Fourier spaces to the boundary $x = x_b$ using the method presented in both Refs. [30, 31], allowing one to consider any field distribution at the focus. The solution is then injected as a boundary condition in the ARCTIC code.

Note that the maximum considered pulse energy is 250 nJ. It corresponds to an initial pulse power of 1.82 MW, which is below the critical power $P_{cr} = 2.8$ MW for self-focusing in fused silica [32]. To decrease the numerical cost of simulations, the nonlinear dielectric susceptibility $\chi^{(3)}$ is thus neglected in Eq. (12).

The numerical box size for simulations is 20 $\mu m$ along the propagation direction $x$, and 16 $\mu m$ in both transverse directions $y$ and $z$. The spatial resolution of 5 nm and temporal resolution of 0.05 fs insure the numerical convergence. The laser boundary conditions are located at $x_b = -14.5$ $\mu m$, and $x = 0$ corresponds to the focal plane, accounting for the fused silica refractive index.

The PFT in the focal plane could be represented by several parameters, like $Q_{zt}$ or $\gamma$. For this purpose, the asymptotic temporal stretch $\alpha_\infty$ is now introduced, and defined as the enhancement factor of the pulse duration $\tau(x)|_{x \gg x_R}/\tau_0$, at infinite distance from the focal plane

$$\alpha_\infty = 1/\sqrt{\gamma}. \tag{17}$$

**Table 1. Laser and material parameters used in simulations [27, 33]**

| Parameter | Symbol | Value |
|---|---|---|
| Laser wavelength | $\lambda_0$ | 800 nm |
| FWHM beam waist | $\sqrt{2\ln 2}w_0$ | 1 $\mu$m |
| FWHM pulse duration | $\sqrt{2\ln 2}\tau_0$ | 150 fs |
| Material density | $\rho_0$ | 2.2 g/cm$^3$ |
| Refractive index | $n_0$ | 1.45 |
| Band gap | $U_g$ | 9 eV |
| Lattice heat capacity | $C_l$ | 1.6 J/cm$^3$/K |
| Linear susceptibility | $\chi^{(1)}$ | 1.11 |
| Recombination time | $\tau_r$ | 150 fs |
| Electron collision frequency | $\nu_e$ | 3 fs$^{-1}$ |
| Electron-lattice relaxation time | $\tau_{el}$ | 1 ps |

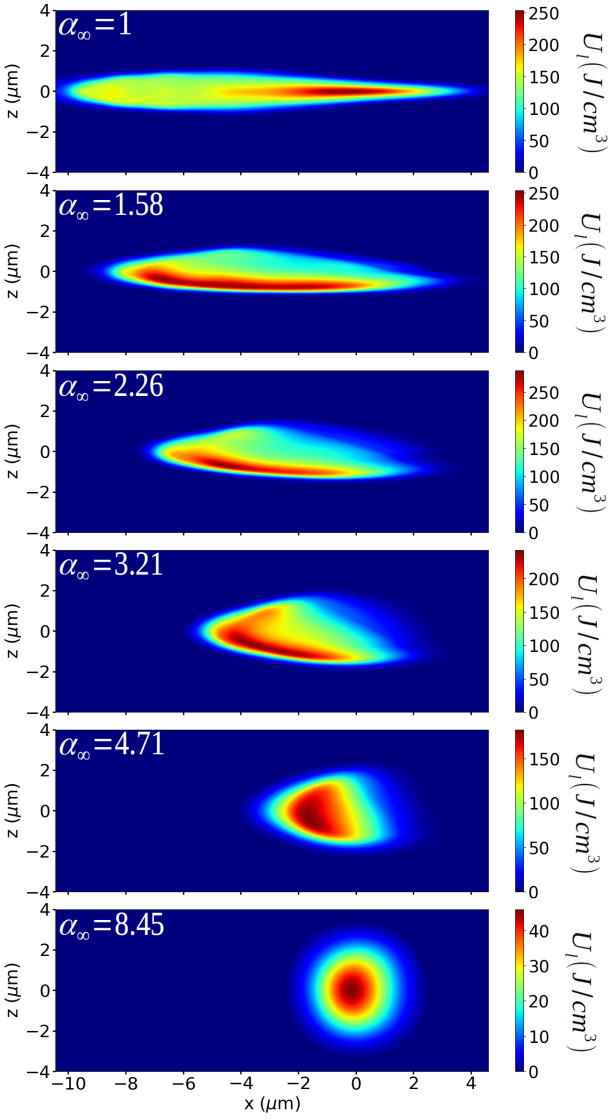


**Fig. 4.** Spatial distribution of the final lattice energy density in the (x,z) domain, for different temporal stretches $\alpha_\infty$ achieved during spatiotemporal focusing, and for a 1 $\mu$m, 150 fs and 180 nJ laser pulse.

It pertains to an experimental observable since it represents the ratio between the pulse duration before the focusing lens of the system and the pulse duration in the focal plane. In the following, this quantity will be used as a parameter representing $Q_{zt}$ and thus the PFT, for given waist and duration.

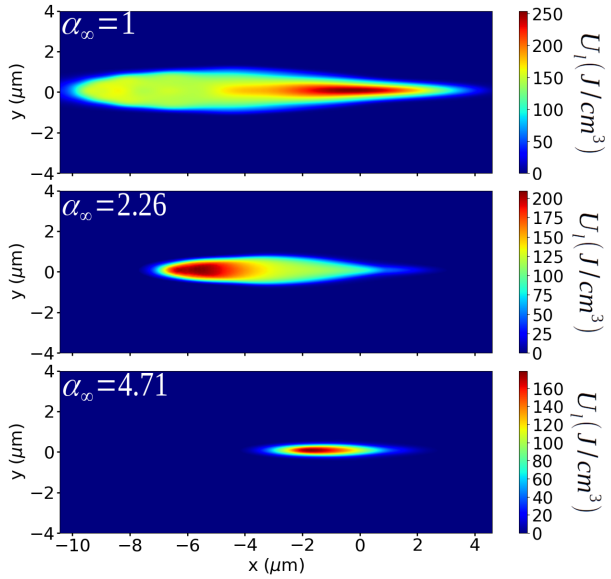


**Fig. 5.** Spatial distribution of the final lattice energy density the (x,y) domain at $z = 0$, for $\alpha_\infty = 1$, 2.26, and 4.71 achieved during SSTF, and for a 1 $\mu$m, 150 fs and 180 nJ energy laser pulse.

### A. Spatiotemporal coupling effect

In this section, the influence of the PFT on the laser energy absorption is studied, depending of the incident pulse energy. For this purpose, pulse energies $W_1 \simeq 125$ nJ, $W_2 \simeq 180$ nJ and $W_3 \simeq 250$ nJ are considered. For each pulse, the influence of the PFT is studied by varying $\alpha_\infty$. For an incident laser energy $W_p$, the corresponding maximum laser intensity $I_p$ at the focal point is obtained by using Eq. (5),

$$I_p = (2/\pi)^{3/2} W_p / w_0^2 \tau_0 \alpha_\infty, \tag{18}$$

and decreases with increasing $\alpha_\infty$ due to the spatial stretch in the (x,z) plane induced by the spatiotemporal coupling term (see Figs. 2 and 3). For a given initial laser energy, the maximum laser intensity $I_p$ is lower for spatio-temporally focused laser pulse than for a simple gaussian pulse. For the considered pulse energies, the related peak intensities in the focal plane for the different $\alpha_\infty$ values used in the simulations, are reported in Tab. 2. The temporal enhancement factor $\alpha$ at $x_b$, is also shown to make clear the difference with $\alpha_\infty$. In the present study, the PFT angle $\theta_{PFT}$ can reach large values compared with the literature, since it scales as $\tau_0/w_0$ and because a relatively long pulse duration is considered. With $\theta_{PFT}$ approaching $\tau_0/w_0$, $\alpha_\infty$ continue to increase. In this work, the maximum value is $\alpha_\infty = 8.45$ with $\theta_{PFT} = 170$ fs/$\mu$m. The experimental work [8] reports $\alpha_\infty \simeq 20$, for similar numerical aperture and half lower pulse duration, corresponding to $\theta_{PFT} = 60$ fs/$\mu$m. The higher angle in the present study is related to the longer pulse duration, but the low value of $\alpha_\infty$ indicates this configuration should be achievable.

The spatial distribution of the final lattice energy density in the $(x,z)$ domain at $y = 0$ is presented in Fig. 4 for a 180 nJ pulse energy (corresponding to $I_2$ intensities in Tab. 2 for a

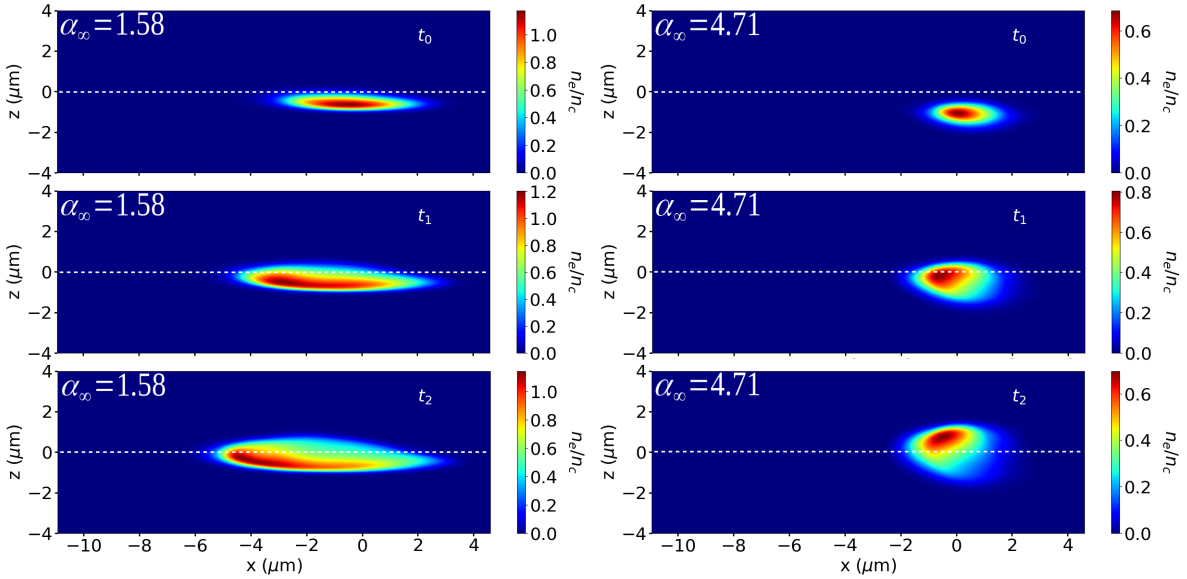


**Fig. 6.** Temporal evolution of the electron density for the 180 nJ laser pulse, with $\alpha_\infty = 1.58$ (left) and $\alpha_\infty = 4.71$ (right). The time $t_0$ corresponds to the time where the peak of the pulse reach the boundary of the domain at $x_b = -14.5\ \mu m$, $t_1 = t_0 + \alpha_\infty \tau_0/4$ and $t_2 = t_0 + \alpha_\infty \tau_0/2$. The pulse propagates from left to right, the propagation axis is indicated by the horizontal dashed line.

**Table 2. Spatiotemporal coupling term $Q_{zt}$ (in fs$^{-1}\mu$ m$^{-1}$), and the associated asymptotic temporal stretch $\alpha_\infty$, temporal enhancement factor $\alpha$ at $x_b = -14.5\ \mu$m, and maximum laser intensities (in TW/cm$^2$) corresponding to pulse energy of 125, 180 and 250 nJ, used in the simulations.**

| $Q_{zt}$ | $\alpha_\infty$ | $\alpha$ | $I_1$ | $I_2$ | $I_3$ |
|---|---|---|---|---|---|
| 0 | 1 | 1 | 68.5 | 100 | 137 |
| 7.15 $10^{-3}$ | 1.58 | 1.5 | 43.5 | 63.5 | 87 |
| 8.31 $10^{-3}$ | 2.26 | 2 | 30 | 44 | 60 |
| 8.80 $10^{-3}$ | 3.21 | 2.5 | 21 | 31 | 42 |
| 9.05 $10^{-3}$ | 4.71 | 3 | 14 | 20 | 28 |
| 9.20 $10^{-3}$ | 8.45 | 3.5 | 10 | 14 | 20 |

linear propagation) and various values of $\alpha_\infty$. Note that the intensity in Eq. (18) corresponds to linear approach, where Fig. 4 description refers to nonlinear. The maximum final lattice energy density decreases as the temporal stretch increases due to the decrease of the maximum laser intensity. For the gaussian beam ($\alpha_\infty = 1$), the spatial distribution of final lattice energy exhibits the well known tear-shaped energy deposition [34, 35]. With the laser energy increasing, the beam cross section where the laser fluence is equal to the threshold value shifts backward the beam propagation direction. The ionized matter volume is stretched upstream of the focal point resulting in an elongated energy absorption volume.

Increasing $\alpha_\infty$ in Fig. 4 leads to reduce the stretching of the energy absorption volume along the propagation axis, while its transverse dimension becomes larger. It also produces an asymmetric energy distribution with respect to the $(x, z)$ plane. As the maximum laser intensity is lower due to the PFT, the motion of the ionization front backward the laser pulse propagation direction is reduced. At the same time, the spatial stretch of the laser pulse due to the spatiotemporal coupling, induces an expansion of the ionized matter volume along the PFT direction.

To explain the observed asymmetry of energy deposition in Fig. 4, the evolution of the electronic density $n_e(x, z)$ at $y = 0$ during the laser pulse propagation for $W_2$ and $\alpha_\infty = 1.58$ (left panels) and 4.71 (right panels) is presented in Fig. 6. The electron density is normalized to the critical density $n_c = 1.7 \times 10^{21}$ cm$^{-3}$. Time $t_0$ corresponds to the time where the peak laser intensity is at $x_b$ (left boundary of the simulation box), $t_1 = t_0 + \alpha_\infty \tau_0/4$ and $t_2 = t_0 + \alpha_\infty \tau_0/2$. Before $t = t_0$, the electron density develops at the same position, with much lower value. After $t = t_2$, the electron density starts to fall. Note that considered times are different, longer for $\alpha_\infty = 4.71$, due to the longer pulse duration at $x_b$. For $\alpha_\infty = 1.58$, $t_1 = t_0 + 50$ fs and $t_2 = t_0 + 100$ fs. For $\alpha_\infty = 4.71$, $t_1 = t_0 + 150$ fs and $t_2 = t_0 + 300$ fs.

In both cases in Fig. 6, the ionization process starts in the region $z < 0$ because of the PFT sign. At the focal spot, the ionization threshold has been reached well before the peak intensity of the laser pulse crosses the focal plane. For $\alpha_\infty = 1.58$, the ionization starts closer to the optical axis due to the lower PFT. The critical density is already reached for $t_0$, between $x = -2\ \mu$m and 1.5 $\mu$m. Thereafter, the ionized region is shifted toward the laser source like in the case of a gaussian pulse (see Fig. 4). Because of the high electron density, and its vicinity with the optical axis, the pulse propagation is strongly affected. The tail of the laser pulse is defocused by the ionized matter. Consequently the field in the region $z > 0$, corresponding to the latter part of the laser pulse, produces fewer electron and undergoes smaller absorption, leading to the asymmetric energy deposition observed in Fig. 4. This result is in agreement with the counter-intuitive observation reported in [13], where a strongly asymmetric interaction is observed even if the PFT is small.

For $\alpha_\infty = 4.71$ in Fig. 6, the electron density is lower at $t_0$ and the ionized matter volume is farther below the optical axis and closer to the focal plan, because of the high PFT angle and lower maximum intensity. For longer times, the ionized region moves over the optical axis leading to a more symmetric energy deposition (see Fig. 4). The maximum electron density is always lower than $n_c$ in the ionized matter, and the defocusing of the laser pulse tail is lower.

In the $(x, y)$ domain, the absorption volume is always symmetric like in the gaussian case (see Fig. 5). However, a decrease of the absorption volume is obtained due to the lower maximum laser intensity, while the position of the maximum final lattice energy is moved toward the front of the tear shape, as it was explain previously. The 3D shape of the affected volume corresponds to an ellipsoid which characteristic size in the $y$ direction is significantly shorter than the one in the two other directions.

Figure 7 presents (a) the total absorbed energy by the lattice $W_{abs}$, (b) the affected volume $V_{eff}$, (c) the effective absorbed energy density by the lattice $U_{eff}$ and (d) the transverse asymmetry of the affected volume as a functions of the temporal stretch $\alpha_\infty$ for the three considered incident pulse energies. The total absorbed energy $W_{abs}$ is normalized by the incident pulse energy, and the effective volume of interaction $V_{eff}$ corresponds to the material volume where the absorbed density is larger than 100 J/cm$^3$. The effective absorbed energy density by the lattice corresponds to the ratio of the total absorbed energy by the lattice in the volume $V_{eff}$ and $V_{eff}$. The transverse asymmetry of the impacted region is defined as the relative difference of the deposited energy between the region $z < 0$ and $z > 0$. A positive asymmetry indicates that more energy is deposited in the region $z < 0$, where the pulse first arrives. Note that the 100 J/cm$^3$ value considered to determine $V_{eff}$ is much lower than the threshold value required to induce significant modification ($\approx$ 2.5 kJ/cm$^3$ [36]), due to the considered focusing conditions. A short burst of twenty pulses with a picosecond delay could be employed to reach the threshold [37].

For each temporal stretch, the relative absorbed energy by the lattice $W_{abs}/W_p$ (Fig. 7(a)) increases with the incident energy, and for a fixed $W_p$ value, it decreases with the increase of $\alpha_\infty$. The same trend is observed for the affected volume $V_{eff}$ (Fig. 7(b)). For a given temporal stretch, increasing $W_p$ leads to increase the laser intensity $I_p$. Like for the gaussian beam, the ionized volume is stretched upstream of the focal point, while its transverse size increases. The absorption volume is wider, and the absorbed laser energy increases. However, for a considered incident energy, the maximum laser intensity decreases with increasing $\alpha_\infty$. In this case, the ionized volume decreases, leading to a lower laser energy absorption in the material.

For the three considered laser energy, the effective absorbed energy density by the lattice $U_{eff}$ (Fig. 7(c)), first increases and reaches a maximum which depends on the pulse energy. Then, it decreases, more sharply for lower pulse energy. This result indicates that the decrease of the total absorbed energy by the lattice with $\alpha_\infty$ can be compensated by the decrease of the impacted volume. Therefore, depending on the pulse energy, the localized energy deposition can be improved compared with the gaussian case using a chirped pulse, without any further intensity localisation.

The transverse asymmetry of the absorption volume is defined as $W_{inf}/W_{sup} - 1$, where $W_{inf}$ and $W_{sup}$ are the total absorbed energy by the lattice in the regions $z < 0$ and $z > 0$, respectively. It is shown in Fig. 7(d). It increases up to 12% when a spatiotemporal coupling is introduced whatever the incident laser pulse energy. Thereafter, the asymmetry decreases as the temporal stretch increases. This decrease is sharper for lower pulse energy. As it was explain previously, this asymmetry is introduced by the matter ionized by the first part of the laser pulse which disturbs the propagation of the laser pulse tail. This effect is stronger for small $\alpha_\infty$ due to the higher maximum laser intensity. Note that the asymmetry for the gaussian pulse is not zero because of the spatial resolution of the numerical simulations.

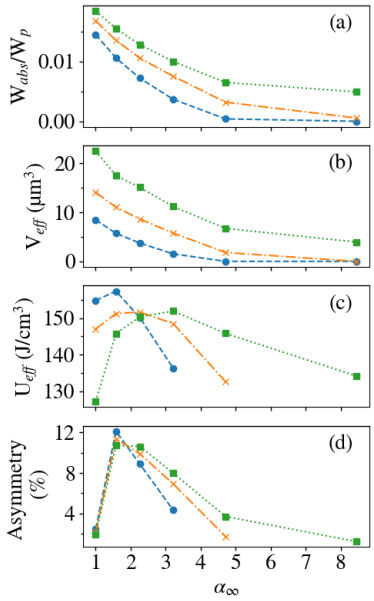


**Fig. 7.** Evolution of (a) absorbed laser energy, (b) maximum absorbed energy density by the lattice, (c) effective volume, (d) effective absorbed energy density by the lattice and (e) asymmetry with the temporal stretch $\alpha_\infty$. The blue rounds corresponds to $W_1 = 125$ nJ, the orange crosses to $W_2 = 180$ nJ and the green squares to $W_3 = 250$ nJ. The lines are guides to the eyes.

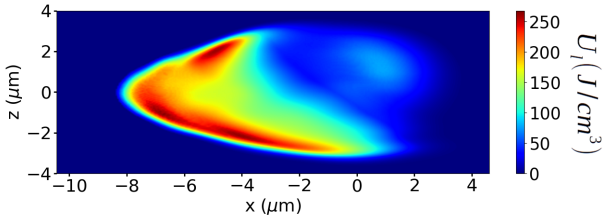


**Fig. 8.** Spatial distribution of the absorbed energy density the (x,z) domain, for $\alpha_\infty = 4.71$, for a 1 $\mu$m, 150 fs, 50 TW/cm$^2$ laser pulse.

These results show that using a high PFT leads to a better energy confinement near the focal point. However, if the incident pulse energy is increased, the energy deposition area becomes also highly inhomogeneous and asymmetric with a PFT (see Fig. 8 where $W_p = 310$ nJ and $\alpha_\infty = 4.71$). The better confinement obtained previously was induced by the maximum laser intensity decrease with the PFT increase. In order to control the aspect ratio of the structure, it is clear that higher values of $\alpha_\infty$ restricts the intensity to near interaction threshold values.

It is worth-noting that the influence of the WFR was not discussed in our analysis, as well as the group delay dispersion (GDD) introduced by the material, which itself contributes to the WFR. Indeed, even if the electric field in the focal plane only presents a PFT (see Eq. (2)), a WFR exists for any other longitudinal position (see Eq. (4)). The absence of both WFR and GDD in our analysis should be justified regarding our laser configuration. First, it was checked that the PFT angles in the focal plane ($x = 0$) and at the domain boundary ($x = x_b$), are the same, due to the short distance between these positions. The rotation of the wave-front is observed only far from the focal plane ($x \gg x_R$). For this reason, the WFR do not play any role in the asymmetric interaction in the present configuration, contrary

to the results presented in Ref. [14]. The GDD can be evaluated from the group velocity dispersion (GVD), i.e the GDD per unit length. The GVD coefficient of fused silica is $k_2 = 35$ fs$^2$/mm for $\lambda_0 = 800$ nm [38]. The characteristics length for GDD can thus be evaluated as $\tau_0^2/k_2 \simeq 460$ mm, which is significantly longer than the 20 $\mu$m propagation distance considered in this study.

### B. Controlling the aspect ratio of the absorbing region

From the previous section, it appears that the lower the pulse energy, the more homogeneous the absorbing region (see figures 4 and 8). This suggests that homogeneous impacted area are expected close to the ionization intensity threshold. Within this configuration, the aspect ratio of the area, i.e. the ratio of its length along the $x$ axis (laser propagation axis) to its width along the $z$ axis (chirp axis), can be properly defined, contrary to Sec. A where the inhomogeneous energy deposition prevented from this definition. This section is mainly devoted to study the evolution of this aspect ratio with respect to the laser intensity near the material interaction threshold. For fused silica, this threshold intensity is around 20 TW/cm$^2$ [4, 27]. This value is in agreement with the present numerical simulations. In Fig. 9, the absorbed laser energy density $U_l$ is presented in the $(x, z)$ domain for $y = 0$, $\alpha_\infty = 1$, 4.71 and 8.45, and $I_p = 20$ TW/cm$^2$. Like previously, the absorbing region is referenced as the area where $U_l$ is larger than 100 J/cm$^3$. Its length is measured on the optical axis and its width corresponds to the maximum transverse dimension (see Fig. 9 for $\alpha = 8.45$). The width of the absorbing region is increased with increasing $\alpha_\infty$ due to the larger PFT, while its length is shortened due to the pulse duration evolution that modify the longitudinal fluence evolution. Furthermore, the maximum of energy deposition is reduced.

Figure 10 presents (a) the total absorbed energy by the lattice, (b) the effective volume of interaction, (c) the effective absorbed energy density by the lattice and (d) the asymmetry as functions of $\alpha_\infty$, like in Fig. 7, but for the three maximum laser intensities $I_p = 18$, 20 and 22 TW/cm$^2$. $W_{abs}$ increases with the maximum laser intensity for all $\alpha_\infty$ values. Increasing $I_p$ leads to increase the ionized matter volume, then the laser absorption volume and $V_{eff}$ (see Fig. 10(b)). However, for a fixed maximum laser intensity, $W_{abs}$ starts to decrease when the temporal stretch is introduced, and then increases with $\alpha_\infty$. At the same time, the $V_{eff}$ increase due to the PFT leads to increase the total absorbed energy by the lattice with the temporal stretch. Note that the minimum of $W_{abs}/W_p$ corresponds to the maximum asymmetry, and can be attributed to the higher defocusing for low PFT. The effective absorbed energy density by the lattice $U_{eff}$ (Fig. 10(c)) decreases with $\alpha_\infty$, up to a saturating value. This behavior, very different from Sec. A, is due to the relative increase of the effective volume, which is greater than the relative increase of the total absorbed energy. This indicates that near the interaction threshold, the PFT tends to limit the localization due to the large increase of the volume of interaction. The asymmetry evolution in Fig. 10(d) is similar to the previous case where constant laser pulse energy was considered. However, the absorbing area is much more homogeneous. The asymmetry increases up to a maximum value when $\alpha_\infty \simeq 1.5$ for the three considered laser intensities. For larger $\alpha_\infty$, the asymmetry decreases. For the smaller values of $\alpha_\infty$, the PFT angle is small and the ionization starts closer to the optical axis. The laser pulse propagation is disturbed by the ionized matter like in the previous section, even if the maximum laser intensities are close to the threshold intensity. When $\alpha_\infty$ increases, the PFT angle increases, and the laser pulse tail is less disturbed by the conduction electrons resulting from ionized matter by the laser pulse front.

Figure 11 presents the evolution of (a) the width $L$, (b) the length $l$ (see Fig. 9) and (c) the aspect ratio $R = l/L$ of the absorbed energy domain as a function of the temporal stretch $\alpha_\infty$ for $I_p = 18$, 20 and 22 TW/cm$^2$. For the considered laser intensities, the width of the absorption area almost linearly increases with $\alpha_\infty$ due to the PFT inducing the higher transverse extension of the effective radius in the direction of the tilt (see Fig. 3).

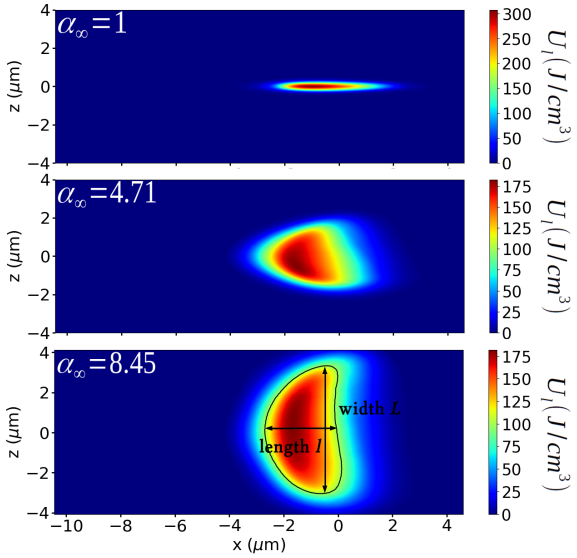


**Fig. 9.** Spatial distribution of final lattice energy density in the $(x, z)$ domain for different temporal stretches $\alpha_\infty$, for a 1 $\mu$m, 150 fs, 20 TW/cm$^2$ intensity laser pulse. Both the length $l$ and the width $L$ are shown for $\alpha_\infty = 8.45$. The black line corresponds to $U_l = 100$ J/cm$^2$.

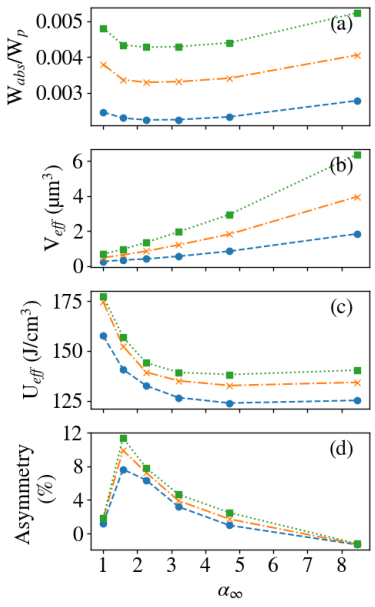


**Fig. 10.** Evolution of (a) total absorbed energy by the lattice, (b) maximum absorbed energy density by the lattice, (c) affected volume, (d) effective absorbed energy density by the lattice and (e) asymmetry with the temporal stretch $\alpha_\infty$. The blue rounds corresponds to $I_p = 18$ TW/cm$^2$, the orange crosses to $I_p = 20$ TW/cm$^2$ and the green squares to $I_p = 22$ TW/cm$^2$.

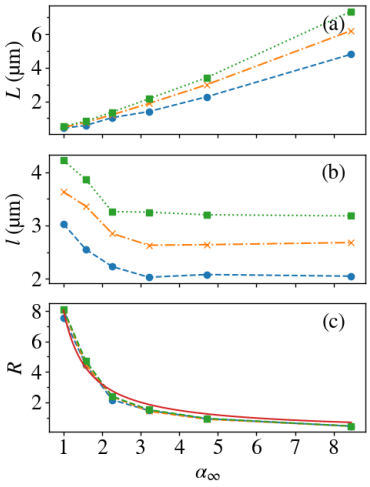


**Fig. 11.** Dependence to the temporal stretch $\alpha_\infty$ of the modified material width (a), length (b) and aspect ratio (c) for various pulse intensities around the interaction threshold. The blue rounds corresponds to $I_1 = 18$ TW/cm$^2$, the orange crosses to $I_2 = 20$ TW/cm$^2$ and the green squares to $I_3 = 22$ TW/cm$^2$. The red curve in (c) corresponds to the theoretical aspect ratio obtained from Eq. (19).

At the same time, the length of the absorption area decreases with the increase of the temporal stretch $\alpha_\infty$ because of the higher energy absorption taking place for longer pulse duration. For values of $\alpha_\infty$ larger than 3.21, the pulse duration evolution becomes independent of $\alpha_\infty$ since it corresponds to $\gamma \ll 1$ (see Eq. (7)), and the only remaining effect on the aspect ratio is the increase of the beam transverse dimension due to the PFT. The aspect ratio $R$ of the structure presented in Fig. 11(c) quickly decreases with increasing $\alpha_\infty$, but is almost independent of the laser intensity for the considered intensities. For near threshold intensities, the diminution of the aspect ratio is mostly due to the PFT which increases the width of the absorption area rather than the higher absorption that shortens its length. For the gaussian pulse $R \simeq 8$, and for $\alpha_\infty = 8.45$ $R \simeq 0.5$, which is a variation of more than one order of magnitude. An aspect ratio $R \simeq 1$ is achieved for $\alpha_\infty = 4.71$. For lower numerical aperture, one can expect larger width of the absorption volume along the PFT direction. By keeping $\alpha_\infty$ constant, a lower numerical aperture would also results in longer length along the propagation axis, but with the same aspect ratio. For higher numerical aperture, polarization effects and directional writing are expected [17]. Furthermore, a higher absorption of the pulse energy and smaller energy deposition area would be achieved.

For application or experiment design purposes, an analytical expression of the aspect ratio of the laser induced structure can be derived. A rigorous derivation is not straightforward because the length depends on the pulse duration [27]. An ad'hoc approach is thus used and predictions compared with previous full numerical simulations allow us to validate a posteriori the proposed analytical expression of the aspect ratio. The linear dependence of the structure width with $\alpha_\infty$ (see Fig. 10(a)) suggests that the effective waist $w_{eff} = \alpha_\infty w_0$ in Eq. (9) correctly evaluates the behavior of increasing transverse structure size due to the PFT. Note that $w_{eff}$ is intensity-independent since it is defined as the 1/e transverse extension of the fluence profile. A test function for $x_{eff}$ is given by $x_{eff} = \sqrt{(1+\gamma)/2}x_R$. The aspect ratio defined as $R = x_{eff}/\sqrt{\ln 2/2}w_{eff}$ thus reads :

$$R = \sqrt{\gamma(1+\gamma)/\ln 2}x_R/w_0. \quad \textbf{(19)}$$

As shown by Fig. 11, this expression is in a good agreement with numerical simulations. Finally, note that the aspect ratio is considered within 2D in the $(x,z)$ plane, such that the 3D absorbing region is elongated in the tilt direction $z$. To get a fully 3D symmetric structure, an elliptical beam at the focal spot or a radial chirp [39] could be used.

## 4. CONCLUSION

By studying the propagation of a spatially chirped pulse in vacuum, we have first provided an analytical expression to study the space-time evolution of a femtosecond laser pulse including a spatiotemporal coupling inducing only a pulse front tilt in the focal plane. Thereafter, the propagation of this pulse in fused silica has been studied by numerically solving the Maxwell's equation coupled to the laser induced electron dynamics. The distribution of the energy deposition in the volume of fused silica has been obtained for different incident laser energy and coupling parameter values. These qualitative results show that the spatiotemporal coupling leads a better confinement near of the focal point of the deposited energy volume in the material than by using a classical gaussian pulse with the same energy. Due to the PFT, the maximum laser intensity is lower and the ionized volume is closer to the focal point. However, by increasing the incident laser energy, the deposited energy volume becomes asymmetric with respect to the propagation axis. Finally, the energy deposition volume has been studied for near threshold maximum laser intensities and different coupling values. It has been shown that the pulse front tilt allows one to decrease the aspect ratio (length over width) of the absorbing area relative to conventional gaussian beam, up to one order of magnitude. For application purposes, we have proposed a simple analytical expression to evaluate the aspect ratio of the structure depending of the spatio-temporal coupling value. To conclude, tilted laser pulses add a degree of freedom to the conventional Gaussian beam, and offer a possibility to control and design the shape of laser induced bulk modifications. A final comment should be made concerning the fundamental importance of the pulse duration. In this study, the spectral chirp was neglected regarding the 150 fs pulse duration and the considered chirp parameters [10]. In this case the field at the focus only presents a PFT (see Eq. (2)). This is not true for shorter pulse duration, where the spectral chirp would be responsible for further longitudinal intensity localization [10]. This would probably result in a smaller length and lower aspect ratio of the absorbing area, and a potential increase of the absorbed energy. Furthermore, for a 150 fs pulse duration, the wavelength range is small enough to insure the validity of the Keldysh model. Shorter pulse duration could not satisfy this condition, and time-dependent ionization model would have to be introduced for the simulations [40].

## 5. FUNDING INFORMATION

We acknowledge the Aquitaine Regional Council for support and funding via the SIMULER project. This work was granted access to the HPC resources of TGCC under the allocation A0030506129 made by GENCI and the allocation 2017174175 made by PRACE.

## 6. DISCLOSURES

The authors declare no conflicts of interest.

## REFERENCES


1. K. Sugioka, J. Xu, D. Wu, Y. Hanada, Z. Wang, Y. Cheng, and K. Midorikawa, "Femtosecond laser 3D micromachining: a powerful tool for the fabrication of microfluidic, optofluidic, and electrofluidic devices based on glass," Lab on a Chip **14**, 3447–3458 (2014).
2. R. Stoian, "Volume photoinscription of glasses: three-dimensional micro- and nanostructuring with ultrashort laser pulses," Appl. Phys. A **126**, 438 (2020).
3. E. N. Glezer, M. Milosavljevic, L. Huang, R. L. Finlay, T.-H. Her, J. P. Callan, and E. Mazur, "3-D Optical Storage and Engraving Inside Transparent Materials," in *Ultrafast Phenomena X,* P. F. Barbara, J. G. Fujimoto, W. H. Knox, and W. Zinth, eds. (Springer Berlin Heidelberg, 1996), pp. 157–158.
4. E. G. Gamaly, "The physics of ultra-short laser interaction with solids at non-relativistic intensities," Phys. Reports **508**, 91–243 (2011).
5. R. R. Gattass and E. Mazur, "Femtosecond laser micromachining in transparent materials," Nat. Photonics **2**, 219–225 (2008).
6. A. Patel, Y. Svirko, C. Durfee, and P. G. Kazansky, "Direct Writing with Tilted-Front Femtosecond Pulses," Sci. Reports **7**, 1–14 (2017).
7. F. He, Y. Cheng, J. Lin, J. Ni, Z. Xu, K. Sugioka, and K. Midorikawa, "Independent control of aspect ratios in the axial and lateral cross sections of a focal spot for three-dimensional femtosecond laser micromachining," New J. Phys. **13**, 083014 (2011).
8. G. Zhu, J. v. Howe, M. Durst, W. Zipfel, and C. Xu, "Simultaneous spatial and temporal focusing of femtosecond pulses," Opt. Express **13**, 2153–2159 (2005).
9. R. Kammel, K. Bergner, J. Thomas, R. Ackermann, S. Skupin, and S. Nolte, "Simultaneous spatial and temporal focusing: a route towards confined nonlinear materials processing," in *Laser-based Micro- and Nanoprocessing X,* vol. 9736 (International Society for Optics and Photonics, 2016), p. 97360T.
10. C. G. Durfee, M. Greco, E. Block, D. Vitek, and J. A. Squier, "Intuitive analysis of space-time focusing with double-ABCD calculation," Opt. Express **20**, 14244–14259 (2012).
11. S. Akturk, X. Gu, P. Gabolde, and R. Trebino, "The general theory of first-order spatio-temporal distortions of Gaussian pulses and beams," Opt. Express **13**, 8642–8661 (2005).
12. S. Zhang, D. Asoubar, R. Kammel, S. Nolte, and F. Wyrowski, "Analysis of pulse front tilt in simultaneous spatial and temporal focusing," JOSA A **31**, 2437–2446 (2014).
13. V. P. Zhukov, S. Akturk, and N. M. Bulgakova, "Asymmetric interactions induced by spatio-temporal couplings of femtosecond laser pulses in transparent media," JOSA B **36**, 1556–1564 (2019).
14. Y. Li, J. Song, J. Song, Q. Zhai, W. Yin, X. Tang, and Y. Dai, "Effect of wavefront rotation on the photoionization process by ultrafast laser spatiotemporal focusing," JOSA B **38**, 1040–1047 (2021).
15. F. He, Z. Wang, B. Zeng, J. Ni, W. Chu, K. Sugioka, and Y. Cheng, "Three-dimensional patterning in transparent materials with spatiotemporally-focused femtosecond laser pulses," in *Optoelectronic Imaging and Multimedia Technology III,* vol. 9273 (International Society for Optics and Photonics, 2014), p. 927316.
16. R. Beuton, B. Chimier, P. Quinoman, P. González Alaiza de Martínez, R. Nuter, and G. Duchateau, "Numerical studies of dielectric material modifications by a femtosecond Bessel–Gauss laser beam," Appl. Phys. A **127**, 334 (2021).
17. A. Patel, V. T. Tikhonchuk, J. Zhang, and P. G. Kazansky, "Non-paraxial polarization spatio-temporal coupling in ultrafast laser material processing," Laser & Photonics Rev. **11** (2017).
18. O. D. Caulier, K. Mishchik, B. Chimier, S. Skupin, A. Bourgeade, C. J. Léger, R. Kling, C. Hönninger, J. Lopez, V. Tikhonchuk, and G. Duchateau, "Femtosecond laser pulse train interaction with dielectric materials," Appl. Phys. Lett. **107**, 181110 (2015).
19. P. González de Alaiza Martínez, G. Duchateau, B. Chimier, R. Nuter, I. Thiele, S. Skupin, and V. T. Tikhonchuk, "Maxwell-consistent, symmetry- and energy-preserving solutions for ultrashort-laser-pulse propagation beyond the paraxial approximation," Phys. Rev. A **98**, 043849 (2018).
20. K. Yee, "Numerical solution of initial boundary value problems involving maxwell's equations in isotropic media," IEEE Transactions on Antennas Propag. **14**, 302–307 (1966).
21. J.-P. Berenger, "Three-Dimensional Perfectly Matched Layer for the Absorption of Electromagnetic Waves," J. Comput. Phys. **127**, 363–379 (1996).
22. C. Mézel, L. Hallo, A. Bourgeade, D. Hébert, V. T. Tikhonchuk, B. Chimier, B. Nkonga, G. Schurtz, and G. Travaillé, "Formation of nanocavities in dielectrics: A self-consistent modeling," Phys. Plasmas **15**, 093504 (2008).
23. L. V. Keldysh, "Ionization in the field of a strong electromagnetic wave," Sov. Phys. JETP **20**, 1307 (1965).
24. J. R. Peñano, P. Sprangle, B. Hafizi, W. Manheimer, and A. Zigler, "Transmission of intense femtosecond laser pulses into dielectrics," Phys. Rev. E **72**, 036412 (2005).
25. S. S. Nekrashevich and V. A. Gritsenko, "Electronic structure of silicon dioxide (a review)," Phys. Solid State **56**, 207–222 (2014).
26. D. Grojo, M. Gertsvolf, S. Lei, T. Barillot, D. M. Rayner, and P. B. Corkum, "Exciton-seeded multiphoton ionization in bulk SiO2," Phys. Rev. B **81**, 212301 (2010).
27. B. Chimier, O. Utéza, N. Sanner, M. Sentis, T. Itina, P. Lassonde, F. Légaré, F. Vidal, and J. C. Kieffer, "Damage and ablation thresholds of fused-silica in femtosecond regime," Phys. Rev. B **84**, 094104 (2011).
28. N. M. Bulgakova, V. P. Zhukov, S. V. Sonina, and Y. P. Meshcheryakov, "Modification of transparent materials with ultrashort laser pulses: What is energetically and mechanically meaningful?" J. Appl. Phys. **118**, 233108 (2015).
29. P. Audebert, P. Daguzan, A. Dos Santos, J. C. Gauthier, J. P. Geindre, S. Guizard, G. Hamoniaux, K. Krastev, P. Martin, G. Petite, and A. Antonetti, "Space-Time Observation of an Electron Gas in SiO2," Phys. Rev. Lett. **73**, 1990–1993 (1994).
30. N. M. Bulgakova, V. P. Zhukov, Y. P. Meshcheryakov, L. Gemini, J. Brajer, D. Rostohar, and T. Mocek, "Pulsed laser modification of transparent dielectrics: what can be foreseen and predicted by numerical simulations?" JOSA B **31**, C8–C14 (2014).
31. I. Thiele, S. Skupin, and R. Nuter, "Boundary conditions for arbitrarily shaped and tightly focused laser pulses in electromagnetic codes," J. Comput. Phys. **321**, 1110–1119 (2016).
32. G. Fibich and A. L. Gaeta, "Critical power for self-focusing in bulk media and in hollow waveguides," Opt. Lett. **25**, 335–337 (2000).
33. N. M. Bulgakova, R. Stoian, and A. Rosenfeld, "Laser-induced modification of transparent crystals and glasses," Quantum Electron. **40**, 966 (2010).
34. E. G. Gamaly, L. Rapp, V. Roppo, S. Juodkazis, and A. V. Rode, "Generation of high energy density by fs-laser-induced confined microexplosion," New J. Phys. **15**, 025018 (2013).
35. M. Sun, U. Eppelt, W. Schulz, and J. Zhu, "Role of thermal ionization in internal modification of bulk borosilicate glass with picosecond laser pulses at high repetition rates," Opt. Mater. Express **3**, 1716–1726 (2013).
36. I. Iosilevskiy, V. Gryaznov, and A. Solov'ev, "Properties of high-temperature phase diagram and critical point parameters in silica," arXiv:1312.7592 [physics] (2013).
37. C. Gaudiuso, G. Giannuzzi, A. Volpe, P. M. Lugarà, I. Choquet, and A. Ancona, "Incubation during laser ablation with bursts of femtosecond pulses with picosecond delays," Opt. Express **26**, 3801–3813 (2018).
38. R. Paschotta, *Encyclopedia of Laser Physics and Technology* (Wiley-VCH Verlag GmbH, 2008).
39. T. E. Lanier and J. R. Gulley, "Annular Space-Time Focusing in Fused Silica," in *Frontiers in Optics 2015 (2015), paper FTu5E.6,* (Optical Society of America, 2015), p. FTu5E.6.
40. E. Smetanina, P. González de Alaiza Martínez, I. Thiele, B. Chimier, A. Bourgeade, and G. Duchateau, "Optical Bloch modeling of femtosecond-laser-induced electron dynamics in dielectrics," Phys. Rev. E **101**, 063206 (2020).